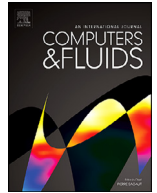




ELSEVIER

Contents lists available at ScienceDirect

Computers and Fluids

journal homepage: www.elsevier.com/locate/compfluid

A non-penetration FEM-MPM contact algorithm for complex fluid-structure interaction problems[☆]

Yan Song, Yan Liu, Xiong Zhang*

School of Aerospace Engineering, Tsinghua University, Beijing 100084, PR China

ARTICLE INFO

Article history:

Received 7 March 2020

Revised 14 July 2020

Accepted 3 September 2020

Available online 6 October 2020

Keywords:

Material point method

Fluid-structure interaction

Particle-surface contact

ABSTRACT

The improved coupled finite element material point (ICFEMP) method is an effective way to deal with fluid-structure interaction problems. However, the FEM-MPM contact algorithm employed in ICFEMP suffers from the contact penetration problem which limits its application in engineering. In this paper, the reason leading to the penetration phenomenon is revealed. The singularity of the normal vector of two adjacent surfaces makes the contact position not well-defined around at the joint line, so that particles near the joint line may penetrate the contact surface. An improved local search method is proposed in this paper to eliminate the penetration. In addition, an iterative process for imposing contact forces is proposed as well to overcome the difficulty that contact conditions can hardly be satisfied simultaneously for all contact pairs caused by the interaction among them. Numerical results illustrate that the proposed contact algorithm thoroughly eliminates the penetration phenomenon even in complex engineering problem such as the airbag simulation.

© 2020 Elsevier Ltd. All rights reserved.

1. Introduction

The material point method (MPM) [1,2] has received increasing attention in recent decades. As a meshless method, the MPM discretizes a material domain as a set of Lagrangian particles moving through an Eulerian background grid. As a result, the MPM combines the benefits of both the Lagrangian method and the Eulerian method. The Eulerian background grid eliminates the mesh distortion problem and the Lagrangian particles trace the free surface of the material domain automatically. The original version of MPM suffers the cell crossing error [3], so different variants have been proposed [3–9] to improve its accuracy. The MPM has been widely used to solve complex problems such as flyer impact [10–15], dynamic fracture [8,16–21], armor piercing [15,22,23], and especially, the fluid-structure interaction (FSI) problem [24,25].

Depending on the solver employed to simulate the fluid and structure regions, there are two main approaches for the FSI simulation [26]: the monolithic approach and the partitioned approach. The monolithic approach simulates the fluid and structure regions with a single solver. Because the momentum equations of the

fluid and structure regions are solved on a common background grid, the MPM ensures the velocity continuity and avoid the penetration naturally. In order to release the bodies which are moving apart, York et al. [24,27] proposed a simple contact algorithm which allows bodies to move in their own velocity fields and the algorithm has been successfully used to simulate the airbag impact. The multi-velocity fields method gets further developed in dealing with FSI problems. Bardenhagen et al. [28,29] introduced the multi-velocity fields in the nodes where contact occurs, thus permitting the slip and separation of different bodies. The multi-velocity fields contact algorithm was improved by Huang et al. [13] which modifies the normal vectors on the contact interface in order to solve the momentum non-conservation problem caused by the non-collinear contact vectors of two contact bodies [28,29]. The multi-mesh method has also been introduced by Hu and Chen [30] to deal with solid contact problems and Ma et al. [12] proposed to employ the local multi-mesh in the contact region in order to lessen the computation burden. Homel [31] and Moutsanidis [32] proposed to enrich the shape function so that the distinct velocity fields are simulated by a single discontinuous velocity field. Cui et al. proposed an alternating finite difference material point (AFDMP) method [33] to model the high explosive explosion and its interaction with structures nearby. The MPM is employed to simulate the initiatory detonation and the eventual fluid structure interaction, while the finite difference method (FDM) is employed to simulate the dispersion of the detonation products into the surrounding air.

[☆] Supported by the National Natural Science Foundation of China (11672154).

* Corresponding author.

E-mail address: xzhang@tsinghua.edu.cn (X. Zhang).

The partitioned approach simulates the fluid and structure region with different solvers and introduces special methods to couple them together. The MPM can be employed to solve the structure part. Guilkey et al. [34] introduced a sub-grid model to close the governing equations and couples the finite-volume method (FVM) region and the MPM region. The coupled finite difference material point (CFDMP) method proposed by Cui et al. [35] couples the FDM fluid and MPM structure regions with a bridging region where the FDM and the MPM exchange information. The immersed boundary (IB) has also been introduced into the MPM to deal with complex boundary. Gilmanov and Acharya [36] proposed a combined hybrid immersed boundary method (HIBM) and MPM approach to solve the FSI problem. The MPM solid structure provides a boundary condition for the volume of fluid (VOF) region and the VOF region impose pressure load to the MPM structure. However, the finite element method (FEM) is more suitable to simulate the solid structure in most circumstances because of its high efficiency and accuracy. Coupling the FEM solid structure and the MPM fluid is a good way to solve the FSI problem. Lian et al. [22] proposed a hybrid finite element material point (HFEMP) method to model the steel reinforced concrete structure where the rebar elements and the concrete particles interact by mapping forces on the background nodes. Hamad et al. [37] extended the HFEMP to model a thin-walled structure in combination with a solid material. The HFEMP is essentially a IB method which can also be applied in FSI simulation.

There is also much research on the contact algorithm between finite elements and material points. Lian et al. [15] proposed a coupled finite element material point method (CFEMP) which introduces a contact algorithm to couple finite elements and material points. However, the contact algorithm in the CFEMP requires consistent meshing between FEM domain and MPM domain, which may result in over-meshing in FEM domain and significantly increases the computational burden. To overcome the difficulty, Cheon and Kim [38] employed distributed interaction nodes on the contact faces of finite elements. Chen et al. [39] proposed an improved particle-to-element contact algorithm to eliminate the consistent meshing, in which the particles contact directly to the surface of finite elements. The ICFEMP method has been successfully used in complex problems. Wu et al. [40] applied the ICFEMP to simulate the bird impact problem. Chen et al. [39] studied the thick plate penetration and the hypothetical core disruptive accident (HCDA) of a fast reactor.

However, the ICFEMP method still suffers from several difficulties. Firstly, the contact penetration phenomenon take place occasionally especially when the contact surfaces are severely deformed. Secondly, the contact forces are imposed on each contact pair. The contact conditions can hardly be satisfied simultaneously because of the interaction among contact pairs. In this paper, we reveal that the penetration phenomenon is caused by the singularity on the joint line of surfaces which leads to nonunique contact vectors in the local search method. Therefore, an improved local search method is proposed to eliminate the singularity. An iterative process of imposing contact forces to find a set of contact forces which make the contact conditions satisfied for every contact pair simultaneously.

This paper is structured as follows. Section 2 gives a brief review of the ICFEMP, including the formulation of the MPM, the FEM and the particle-to-surface contact algorithm. Section 3 analyses the special case which causes the contact penetration and introduces an improved local search method. In Section 4 contact conditions based on the velocity and the displacement are compared and an iterative process for imposing contact forces is developed. Section 5 presents several numerical examples to verify the proposed method.

2. Improved coupled finite element material point method

A brief review of the improved coupled finite element material point method (ICFEMP) is presented in this section. In the ICFEMP, the MPM is usually used to simulate objects with large deformation, while the FEM is usually used to simulate structures with relatively small deformation. The contact algorithm is employed to couple the finite element objects and the material point objects.

The weak form equivalent to the momentum equation and traction boundary condition in the updated Lagrangian frame is given as

$$\int_{\Omega} \rho \dot{\mathbf{u}} \cdot \delta \mathbf{u} dV + \int_{\Omega} \boldsymbol{\sigma} : \nabla (\delta \mathbf{u}) dV - \int_{\Omega} \mathbf{b} \cdot \delta \mathbf{u} dV - \int_{\Gamma_t} \bar{\mathbf{t}} \cdot \delta \mathbf{u} dA = 0 \quad (1)$$

where ρ is the density, \mathbf{u} is the displacement, and $\delta \mathbf{u}$ denotes the virtual displacement, a superimposed dot denotes the time derivative; $\boldsymbol{\sigma}$ is the stress, \mathbf{b} is the specific body force, Γ_t denotes the prescribed traction boundary of the problem domain Ω , and $\bar{\mathbf{t}}$ denotes the prescribed traction on Γ_t .

2.1. The material point method

The MPM discretizes an object by a set of particles which moves on an Eulerian background grid. The particle is essentially an idealization of a small mass of material which only has position and mass and does not take up space [2]. So the density field is approximated by

$$\rho(\mathbf{x}) = \sum_{p=1}^{n_p} m_p \delta(\mathbf{x} - \mathbf{x}_p) \quad (2)$$

where n_p is the total number of particles, m_p is the mass of particle p , \mathbf{x}_p is the coordinates of the particle p and δ is the Dirac Delta function.

The updated Lagrangian frame is employed in this paper. In each time step, material points are fixed on a regular background grid and move and deform along with it. The displacement \mathbf{u}_p of particle p is interpolated from the grid nodes, namely

$$\mathbf{u}_p = \sum_{I=1}^{n_g} N_{Ip} \mathbf{u}_I \quad (3)$$

where n_g is the total number of background grid nodes. \mathbf{u}_I is the displacement of node I . $N_{Ip} = N_I(\mathbf{x}_p)$ is the shape function associated with node I evaluated at the site of particle p . Consequently, the velocity $\dot{\mathbf{u}}_p$ and the virtual displacement $\delta \mathbf{u}_p$ can be obtained by

$$\begin{aligned} \dot{\mathbf{u}}_p &= \sum_{I=1}^{n_g} N_{Ip} \dot{\mathbf{u}}_I \\ \delta \mathbf{u}_p &= \sum_{I=1}^{n_g} N_{Ip} \delta \mathbf{u}_I \end{aligned} \quad (4)$$

Substituting Eqs. (2)–(4) into Eq. (1) gives the nodal momentum equation

$$m_I \dot{\mathbf{u}}_I = \mathbf{f}_I^{\text{int}} + \mathbf{f}_I^{\text{ext}} \quad (5)$$

where m_I is the lumped mass of node I ,

$$\mathbf{f}_I^{\text{int}} = - \sum_{p=1}^{n_p} (\nabla N_{Ip}) \cdot \boldsymbol{\sigma}_p \frac{m_p}{\rho_p} \quad (6)$$

is the grid nodal internal force, $\boldsymbol{\sigma}_p$ is the stress tensor of particle p ,

$$\mathbf{f}_I^{\text{ext}} = \sum_{p=1}^{n_p} \frac{m_p}{\rho_p} N_{Ip} \mathbf{b}_p \quad (7)$$

is the grid nodal external force in which the traction term is omitted for simplicity.

2.2. The finite element scheme

The FEM is usually used to simulate structures with relatively small deformation in the CFEMP. The object is discretized by elements and the displacements of a point with the initial coordinates \mathbf{X} at time t can be approximated as

$$\mathbf{u}(\mathbf{X}, t) = \sum_{K=1}^{n_e} N_K(\xi, \eta, \zeta) \mathbf{u}_K(t) \quad (8)$$

where \mathbf{u} is the displacements, n_e is the total number of nodes, subscript K indicates the variables associated with node K . Substituting Eq. (8) into the weak form Eq. (1) gives the nodal momentum equation

$$M_K \ddot{\mathbf{u}}_K = \mathbf{f}_K^{\text{ext}} + \mathbf{f}_K^{\text{int}} \quad (9)$$

where

$$M_K = \int_{\Omega} \rho N_K dV \quad (10)$$

is the lumped mass of node K ,

$$\mathbf{f}_K^{\text{ext}} = \int_{\Omega} N_K \mathbf{b} dV + \int_{\Gamma_t} N_K \bar{\mathbf{t}} dA \quad (11)$$

is the nodal external force and

$$\mathbf{f}_K^{\text{int}} = - \int_{\Omega} (\nabla N_K) \cdot \boldsymbol{\sigma} dV \quad (12)$$

is the nodal internal force.

The Gauss quadrature is usually employed in the FEM to calculate the integral in Eqs. (10)–(12) which is one of the main difference from the MPM.

2.3. The particle-to-surface contact method

The contact algorithm is employed to couple a finite element object and a material point object. In the contact algorithm proposed by Lian et al. [15], the contact search process relies on the background grid. In each time step, the nodes of FE objects are regarded as particles with mass, momentum and nodal forces which can be mapped to the background grid nodes. The contact occurs if and only if the momentum of a node is contributed by both the FE nodes and the MP particles. This kind of contact algorithm requires that the size of finite element match that of the MPM background grid, namely $L_{\text{FEM}}/L_{\text{MPM}} \approx 1$ where L_{FEM} and L_{MPM} denote the characteristic length of the finite element and MPM background grid cell, respectively. Chen et al. proposed a particle-to-surface contact method to overcome the length requirement and improve the contact accuracy [39]. The contact algorithm is divided into three steps: global search, local search and imposing the contact forces.

The global search is an optional step which searches out the potential contact pairs. A contact pair consists of a finite element face and a material point that are possible to contact each other. The potential contact pairs will be further tested by a local search process to determine whether the contact occurs, which is a time consuming process. Hence, a well-designed global search algorithm is supposed to reduce the number of potential contact pairs as much as possible. The global search algorithm is essentially a space search algorithm which is used to find particles neighboring a finite element face. Many techniques work well to accelerate the global search process such as bucket search [41], position code [42], and the linear octree [43].

The local search process detects the exact contact position on the finite element face for each potential pair and thus calculates

the gap between the face and particle. Consequently, it determines where the contact occurs according to the contact position and the contact gap. Without loss of generality, the finite element face is assumed to be a quadrangle with four nodes $\mathbf{x}_I, I = 1 \dots 4$. The parametric equation of the face is given by

$$\mathbf{x}(\xi, \eta) = \sum_{I=1}^4 N_I(\xi, \eta) \mathbf{x}_I \quad (13)$$

where ξ, η are the natural coordinates ranging from -1 to 1 , N_I is the bilinear shape function

$$N_I(\xi, \eta) = \frac{1}{4} (1 + \xi \xi_I) (1 + \eta \eta_I) \quad (14)$$

The coordinates of the particle in the contact pair is denoted by \mathbf{x}^p . The contact position \mathbf{x}^c is supposed to be the foot of the perpendicular of the particle on to the element face. The tangent vectors of the face can be calculated by

$$\begin{aligned} \mathbf{t}^\xi(\xi, \eta) &= \frac{\partial \mathbf{x}(\xi, \eta)}{\partial \xi} = \sum_{I=1}^4 \frac{\partial N_I(\xi, \eta)}{\partial \xi} \mathbf{x}_I \\ \mathbf{t}^\eta(\xi, \eta) &= \frac{\partial \mathbf{x}(\xi, \eta)}{\partial \eta} = \sum_{I=1}^4 \frac{\partial N_I(\xi, \eta)}{\partial \eta} \mathbf{x}_I \end{aligned} \quad (15)$$

where \mathbf{t}^ξ and \mathbf{t}^η are the tangent vector along the direction that ξ and η increase respectively. As a result, the contact position \mathbf{x}^c and its natural coordinates ξ^c and η^c are supposed to satisfy

$$\begin{aligned} \mathbf{t}^\xi(\xi^c, \eta^c) \cdot (\mathbf{x}^c - \mathbf{x}^p) &= 0 \\ \mathbf{t}^\eta(\xi^c, \eta^c) \cdot (\mathbf{x}^c - \mathbf{x}^p) &= 0 \end{aligned} \quad (16)$$

Eq. (16) can be solved by the Newton–Raphson iterative method. Thus the contact normal \mathbf{n}^c and the contact gap g^c can be calculated as

$$\mathbf{n}^c = \frac{\mathbf{t}^\xi \times \mathbf{t}^\eta}{|\mathbf{t}^\xi \times \mathbf{t}^\eta|} \quad (17)$$

$$g^c = (\mathbf{x}^p - \mathbf{x}^c) \cdot \mathbf{n}^c \quad (18)$$

Two principles must be satisfied if the contact situation occurs on a contact pair. The first principle is that the contact position must locate within the element quadrangle face, namely

$$(\xi^c, \eta^c) \in [-1, 1] \times [-1, 1] \quad (19)$$

The second principle is that the particle must have penetrated into the element. Assume that the element has a thickness d and the radius of the particle is r , then contact gap has to satisfy

$$g^c < \frac{d}{2} + r \quad (20)$$

The next step is to impose contact forces on each validated contact pair. The contact force $F^c \mathbf{n}^c$ between the particle \mathbf{x}^p and the contact position \mathbf{x}^c should be distributed to the finite element nodes and the background grid nodes of the cell where the particle locates in, as shown in Fig. 1. The contact forces $\mathbf{f}_I^e (I = 1 \dots 8)$ on the background grid nodes and $\mathbf{f}_J^e (J = 1 \dots 4)$ on the finite element nodes can be given by

$$\begin{aligned} \mathbf{f}_I^e &= N_{Ip} F^c \mathbf{n}^c \\ \mathbf{f}_J^e &= -N_{Jj}(\xi^c, \eta^c) F^c \mathbf{n}^c \end{aligned} \quad (21)$$

The purpose of the contact force $F^c \mathbf{n}^c$ is to push the particle and the finite element away from each other so that the contact conditions are satisfied. After imposing the contact force on the contact pair, the velocity of the particle p is updated by

$$\mathbf{v}^{p,k+1/2} = \mathbf{v}^{p,k-1/2} + \Delta t^k \sum_{I=1}^8 N_{Ip} \frac{\mathbf{f}_I}{m_I} \quad (22)$$

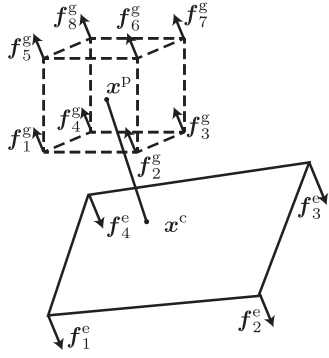


Fig. 1. Imposing contact forces.

where \mathbf{v}^p is the velocity of the particle, Δt^k is the time step, m_l is the mass of the background grid node l and \mathbf{f}_l is its total nodal force. It can be decomposed into the contact force \mathbf{f}_l^g and the original nodal force $\tilde{\mathbf{f}}_l$, i.e.

$$\mathbf{f}_l = \mathbf{f}_l^g + \tilde{\mathbf{f}}_l \quad (23)$$

where

$$\mathbf{f}_l^g = \sum_{p=1}^{n_p} N_{lp} F_p^c \mathbf{n}_p^c \quad (24)$$

and

$$\tilde{\mathbf{f}}_l = - \int_{\Omega} (\nabla N_l) \cdot \boldsymbol{\sigma} dV \quad (25)$$

The velocity of the contact position \mathbf{v}^c can be obtained by interpolating the finite element nodal velocity as

$$\mathbf{v}^c = \sum_{J=1}^4 N_J(\xi^c, \eta^c) \mathbf{v}_J \quad (26)$$

where \mathbf{v}_J indicates the velocity of element node J . The nodal velocity is updated by

$$\mathbf{v}_J^{k+1/2} = \mathbf{v}_J^{k-1/2} + \Delta t^k \frac{\mathbf{f}_J}{m_J} \quad (27)$$

where m_J is the nodal mass. The nodal force has the similar decomposition as Eq. (23),

$$\mathbf{f}_J = \mathbf{f}_J^c + \tilde{\mathbf{f}}_J \quad (28)$$

According to Eq. (21) and Eqs. (22)–(28), the particle and contact position velocity updating formula share a similar expression as

$$\begin{aligned} \mathbf{v}^{p,k+1/2} &= \tilde{\mathbf{v}}^{p,k+1/2} + \Delta t^k F^c \mathbf{n}^c \sum_{l=1}^8 \frac{N_{lp}^2}{m_l} \\ \mathbf{v}^{c,k+1/2} &= \tilde{\mathbf{v}}^{c,k+1/2} - \Delta t^k F^c \mathbf{n}^c \sum_{J=1}^4 \frac{N_J^2}{m_J} \end{aligned} \quad (29)$$

where

$$\begin{aligned} \tilde{\mathbf{v}}^{p,k+1/2} &= \mathbf{v}^{p,k-1/2} + \Delta t^k \sum_{l=1}^8 N_{lp} \frac{\tilde{\mathbf{f}}_l}{m_l} \\ \tilde{\mathbf{v}}^{c,k+1/2} &= \mathbf{v}^{c,k-1/2} + \Delta t^k \sum_{J=1}^4 N_J \frac{\tilde{\mathbf{f}}_J}{m_J} \end{aligned} \quad (30)$$

indicate the predicted velocity which is updated without the contact forces. The contact condition requires the continuity of the velocity of the particle and the contact position in the normal direction, namely

$$\mathbf{v}^{p,k+1/2} \cdot \mathbf{n}^c = \mathbf{v}^{c,k+1/2} \cdot \mathbf{n}^c \quad (31)$$

Substituting Eq. (29) into Eq. (31) results in the resultant contact force

$$F^c = \frac{\tilde{m}_p \tilde{m}_c}{\Delta t^k (\tilde{m}_p + \tilde{m}_c)} \mathbf{n}^c \cdot (\tilde{\mathbf{v}}^{c,k+1/2} - \tilde{\mathbf{v}}^{p,k+1/2}) \quad (32)$$

where the equivalent mass of the particle and the contact position are

$$\begin{aligned} \frac{1}{\tilde{m}_p} &= \sum_{l=1}^8 \frac{N_{lp}^2}{m_l} \\ \frac{1}{\tilde{m}_c} &= \sum_{J=1}^4 \frac{N_J^2}{m_J} \end{aligned} \quad (33)$$

In conclusion, the basic flow of the algorithm is summarized as

1. Use bucket search or other space search method to find out the potential contact pairs.
2. Find the contact position for each potential contact pair, determine its contact situation and calculate the contact normal vector and contact gap.
3. Calculate the predicted velocity and then the resultant contact force.
4. Impose the contact forces on the background grid nodes and the finite element nodes.

3. Improved local search algorithm

In this section, the geometrical features of the local search is analyzed in detail. The contact area of a finite element is defined to describe the space region where a particle is possible to contact. However, the contact area of different elements cannot make up a complete global contact area. Contact cracks between different finite elements causes severe contact penetration phenomenon especially in the fluid problem. We propose an improved local search algorithm to fill up the contact crack and the penetration problem is well solved.

3.1. Contact area and contact crack

Considering the contact criterion Eqs. (19) and (20), the contact occurs only when a particle locates in the region formed through the element extending by a thickness of $d/2$ in the normal direction on each side. The region is defined as ‘contact area’ of the element. Fig. 2 shows the contact area in 3D space and 2D space. Without loss of generality, only 2D schematic will be used to show the geometrical features of the contact area.

When a particle moves into the contact area of a finite element, contact forces will be imposed on the contact pair to push them away. The velocity continuity condition (31) ensures that the contact penetration would not further continue in the next time step. As a result, the contact area prevents particles from going through the finite element face.

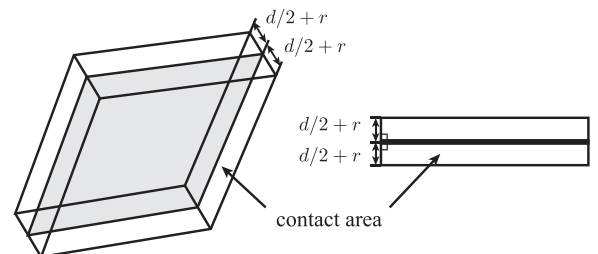


Fig. 2. The contact area. Left is the 3D case where the contact area is a block region. Right is the 2D case where the contact area is a rectangular area.

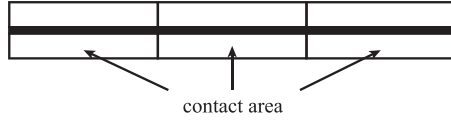


Fig. 3. Flat surface discretized by multi-elements.

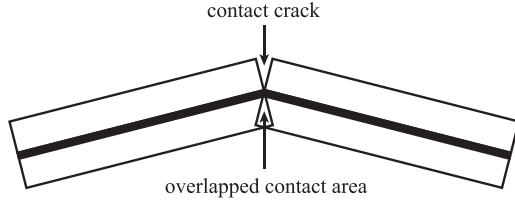


Fig. 4. Contact crack.

The non-penetration condition can also be satisfied when a flat surface is discretized by multi-elements. Fig. 3 shows the global contact area of the elements which compose a flat surface. Apparently a complete global contact area is formed thus the global non-penetration condition is guaranteed. It is noticeable that the normal vectors of the neighboring elements are continuous on the intersecting line of them, which ensures the uniqueness of the foot of a perpendicular.

However, in most circumstances where the normal vectors are not continuous on the intersecting line, the contact area of adjacent elements cannot close. As shown in Fig. 4, the two finite element faces are connected at an angle so that the normal vector is not well defined at the joint point (joint line in 3D space). The contact area of the surfaces overlaps each other on one side but forms an unclosed contact crack on the other side. The contact crack can cause severe penetration problem especially in fluid problem.

In general, the overlapped contact area would not influence the contact property. Particles located in the overlapped contact area are supposed to be detected to contact with both the two surfaces and the contact forces are imposed on the two contact pair.

The contact crack gives rise to the penetration phenomena. When a particle moves into the contact crack, the foots of a perpendicular always fall out of the two surfaces no matter how near they are (see Fig. 5a). Consequently, no contact pair can be detected so that the particle would move through the surfaces and enter the contact area on the other side. Then contact forces will be imposed on the particle to push it toward the other side (see Fig. 5b and c) which leads to penetration. The contact crack appears on the convex side of the joint line of two surfaces and a large number of cracks could appear when the FEM body undergoes large deformation.

3.2. Improved local search algorithm

The contact criterion Eqs. (19) and (20) must be reconsidered to eliminate the contact crack. A particle is supposed to contact with a surface as long as they are close enough. So the contact criterion should tolerate that the contact position is not the foot of a perpendicular in some circumstances and thus the contact vector

should also be modified accordingly. It is reasonable that the contact position lies on the joint point (joint line in 3D space) when the particle locates in the contact crack. However, it is difficult to determine the contact vector because the normal vector of the surface in the contact crack is not well defined.

The contact crack problem is similar with the singular problem of the multiple yield surfaces. Many methods have been proposed to define the gradient on the joint line of yield surfaces. For example, Abbo and Sloan [44] introduced the hyperbolic approximation to smooth the yield surface and Bicanic et al. [45] proposed to define the gradient on the singular point as the linear combination of its neighboring yield surfaces.

To eliminate the contact crack, the contact position \mathbf{x}^c of a particle p is defined as the nearest point on the surface to the particle. Denoting the vector pointing from point \mathbf{x} on the finite element face to particle p as

$$\mathbf{g} = \mathbf{x}^p - \mathbf{x}, \quad (34)$$

the natural coordinates of the contact point $\mathbf{x}^c = \mathbf{x}(\xi^c, \eta^c)$ minimize the magnitude of \mathbf{g} , namely

$$(\xi^c, \eta^c) = \arg \min_{\xi, \eta} \|\mathbf{g}\|^2, \quad (\xi^c, \eta^c) \in [-1, 1] \times [-1, 1] \quad (35)$$

The contact vector \mathbf{g}^c is defined as

$$\mathbf{g}^c = \mathbf{x}^p - \mathbf{x}^c, \quad (36)$$

whose unit vector is the normal vector on the contact position, namely

$$\mathbf{n}^c = \frac{\mathbf{g}^c}{\|\mathbf{g}^c\|} \quad (37)$$

The modified definition of the contact position criterion Eq. (35) can be degenerated into Eq. (16) when the contact position locates in the internal surface. Assuming that

$$(\xi^c, \eta^c) \in (-1, 1) \times (-1, 1), \quad (38)$$

the contact position must be located on the extreme point of $\|\mathbf{g}\|^2$, thus the derivative of $\|\mathbf{g}\|^2$ with respect to natural coordinates ξ, η must satisfy

$$\begin{aligned} \frac{\partial \|\mathbf{g}\|^2}{\partial \xi} \Big|_{(\xi^c, \eta^c)} &= 2\mathbf{g}^c \cdot \frac{\partial \mathbf{x}(\xi^c, \eta^c)}{\partial \xi} = 0 \\ \frac{\partial \|\mathbf{g}\|^2}{\partial \eta} \Big|_{(\xi^c, \eta^c)} &= 2\mathbf{g}^c \cdot \frac{\partial \mathbf{x}(\xi^c, \eta^c)}{\partial \eta} = 0 \end{aligned} \quad (39)$$

Substituting Eq. (15) into Eq. (39) results in

$$\begin{aligned} \mathbf{g}^c \cdot \mathbf{t}^\xi \Big|_{(\xi^c, \eta^c)} &= 0 \\ \mathbf{g}^c \cdot \mathbf{t}^\eta \Big|_{(\xi^c, \eta^c)} &= 0 \end{aligned} \quad (40)$$

which has the same expression as Eq. (16). Eq. (40) signifies that the contact vector is parallel to the normal vector defined by Eq. (17) so that the modified normal vector Eq. (37) can be degenerated into the original expression Eq. (17) on the internal contact position.

When the particle moves into the contact crack, the contact position locates on the joint point (joint line in 3D space) and if the distance criterion Eq. (20) is satisfied, the contact pair would be detected. As a consequence, the contact area extends a semicircle

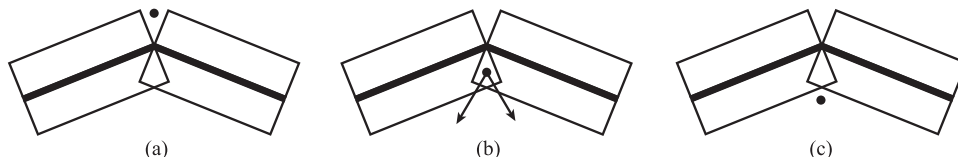


Fig. 5. Penetration process. (a) The particle moves into the contact crack. (b) The particle penetrate the surface and enters the overlapped contact area. (c) The particle are pushed out of the contact area.

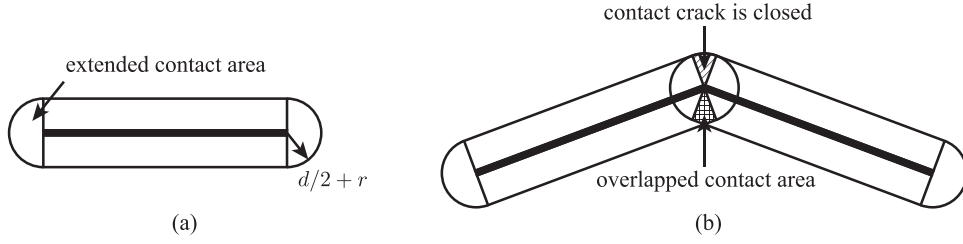


Fig. 6. The modified contact area.

with radius $d/2 + r$ around the joint point as shown in Fig. 6(a). The contact crack is filled by the extended contact area as shown in Fig. 6(b) and the particle in it is detected to contact with the joint point.

3.3. The steepest descent method to solve the contact position

The modified contact positions criterion Eq. (35) is essentially an inequality-constrained optimization problem. Many numerical methods can be employed to solve the contact position such as the quasi-Newton method and the conjugate gradient method. However, because the finite element is usually regular-shaped and lightly-warped, the steepest descent method is able to solve the problem efficiently.

The most important step in the steepest decent method is to calculate the gradient of the objective function $\|\mathbf{g}\|^2$ by

$$\begin{aligned} \frac{\partial \|\mathbf{g}\|^2}{\partial \xi} &= 2\mathbf{g} \cdot \mathbf{t}^\xi \\ \frac{\partial \|\mathbf{g}\|^2}{\partial \eta} &= 2\mathbf{g} \cdot \mathbf{t}^\eta \end{aligned} \quad (41)$$

and the natural coordinates of the contact position is updated by

$$\begin{aligned} \xi^{n+1} &= \xi^n + \alpha \gamma^n \frac{\partial \|\mathbf{g}\|^2}{\partial \xi} \\ \eta^{n+1} &= \eta^n + \alpha \gamma^n \frac{\partial \|\mathbf{g}\|^2}{\partial \eta} \end{aligned} \quad (42)$$

where the superscript n indicates the variables at n th step, γ^n is the step length, $0 < \alpha \leq 1$ is a user-defined parameter. In most circumstances where elements are of small deformation, the iteration converges very fast when α is set around 1.

A regular flat contact surface is considered to estimate the step length. As shown in Fig. 7, $\mathbf{x}(\xi^n, \eta^n)$ is the current coordinates and the contact position \mathbf{x}^c is assumed to be located in the internal surface. $\mathbf{x}(\xi^n, \eta^n)$ is updated by

$$\mathbf{x}(\xi^{n+1}, \eta^{n+1}) = \mathbf{x}(\xi^n, \eta^n) + \gamma^n \frac{\partial \|\mathbf{g}\|^2}{\partial \xi} \mathbf{t}^\xi + \gamma^n \frac{\partial \|\mathbf{g}\|^2}{\partial \eta} \mathbf{t}^\eta \quad (43)$$

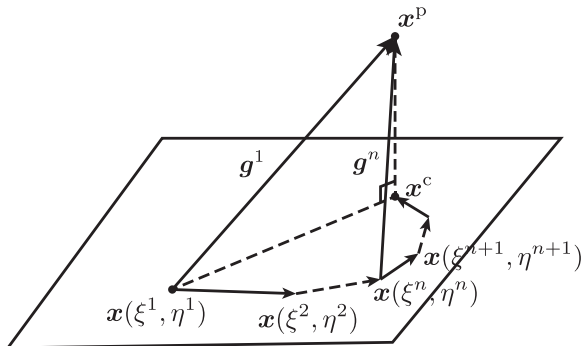


Fig. 7. Steepest descent method.

In order to estimate the optimal step length γ^n , it is assumed that the accurate contact position is reached in one step, namely $\mathbf{x}^c = \mathbf{x}(\xi^{n+1}, \eta^{n+1})$ so that

$$\mathbf{x}^c - \mathbf{x}(\xi^n, \eta^n) = \gamma^n \frac{\partial \|\mathbf{g}\|^2}{\partial \xi} \mathbf{t}^\xi + \gamma^n \frac{\partial \|\mathbf{g}\|^2}{\partial \eta} \mathbf{t}^\eta \quad (44)$$

The geometrical condition requires that

$$\mathbf{g}^n \cdot (\mathbf{x}^c - \mathbf{x}^n) = (\mathbf{x}^c - \mathbf{x}^n) \cdot (\mathbf{x}^c - \mathbf{x}^n) \quad (45)$$

where $\mathbf{x}^n = \mathbf{x}(\xi^n, \eta^n)$. Thereby, γ^n can be solved by

$$\gamma^n = \frac{(\mathbf{g}^n \cdot \mathbf{t}^\xi)^2 + (\mathbf{g}^n \cdot \mathbf{t}^\eta)^2}{2[(\mathbf{g}^n \cdot \mathbf{t}^\xi)^2 \|\mathbf{t}^\xi\|^2 + (\mathbf{g}^n \cdot \mathbf{t}^\eta)^2 \|\mathbf{t}^\eta\|^2]} \quad (46)$$

The convergence criterion is another important part of the local search algorithm. When the contact position locates in the internal surface, the gradient condition Eq. (40) can be used as a convergence criterion, namely

$$\begin{aligned} |\mathbf{g}^n \cdot \mathbf{t}^\xi| &< \varepsilon^\xi \\ |\mathbf{g}^n \cdot \mathbf{t}^\eta| &< \varepsilon^\eta \end{aligned} \quad (47)$$

where ε^ξ and ε^η are extremely small numbers. The criterion can be nondimensionalized as

$$\cos^2 \beta^\xi + \cos^2 \beta^\eta < \varepsilon_1 \quad (48)$$

where ε_1 is a small dimensionless number,

$$\cos \beta^\xi = \frac{\mathbf{g} \cdot \mathbf{t}^\xi}{\|\mathbf{g}\| \|\mathbf{t}^\xi\|}, \quad \cos \beta^\eta = \frac{\mathbf{g} \cdot \mathbf{t}^\eta}{\|\mathbf{g}\| \|\mathbf{t}^\eta\|} \quad (49)$$

are the cosine values of the angles between \mathbf{g} and the tangent vector \mathbf{t}^ξ and \mathbf{t}^η .

Another convergence criterion is also required to deal with the situation where the contact position locates on the joint point. When the coordinates are updated out of the surface region by Eq. (42), they are supposed to be moved to the joint point (joint line in 3D space) by

$$\begin{aligned} \xi^{n+1} &= \begin{cases} 1 & \text{if } \xi^{n+1} > 1 \\ -1 & \text{if } \xi^{n+1} < -1 \end{cases} \\ \eta^{n+1} &= \begin{cases} 1 & \text{if } \eta^{n+1} > 1 \\ -1 & \text{if } \eta^{n+1} < -1 \end{cases} \end{aligned} \quad (50)$$

and then the convergence criterion

$$(\xi^{n+1} - \xi^n)^2 + (\eta^{n+1} - \eta^n)^2 < \varepsilon_2 \quad (51)$$

is employed to further determine if the convergence is reached, where ε_2 is also a small dimensionless number.

In summary, the flow chart of the local search algorithm is shown in Fig. 8.

4. Contact conditions and contact iteration

Contact conditions are reconsidered in this section. Conditions based on the velocity and the displacement are compared and a general formulation of contact force is proposed. The contact conditions can hardly be satisfied for all the contact pairs simultaneously because of their interaction, so an iterative method is proposed to impose the contact forces.

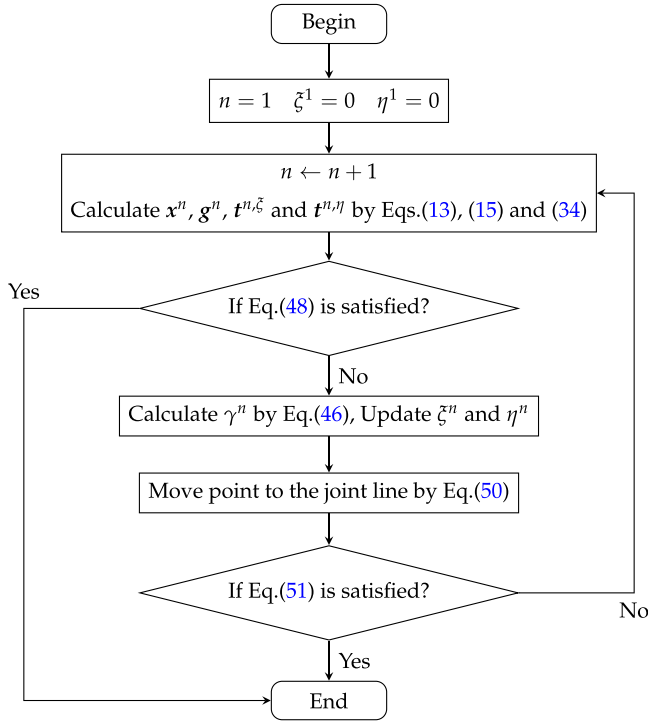


Fig. 8. Flow chart of the local search algorithm.

4.1. Contact conditions analysis

In the contact theory, two contact bodies must satisfy both the displacement and velocity conditions at the contact position. In the CFEMP method, the displacement condition is given by

$$(\mathbf{x}^p - \mathbf{x}^c) \cdot \mathbf{n}^c \geq \frac{d}{2} + r \quad (52)$$

which means the two bodies would not penetrate each other and the velocity condition is given by

$$(\mathbf{v}^p - \mathbf{v}^c) \cdot \mathbf{n}^c \geq 0 \quad (53)$$

which represents the penetration trend is stopped by the contact force. The equality in Eqs. (52) and (53) are reached simultaneously. The contact forces can be given based on each of the conditions. Because the contact process finishes when the contact bodies move apart, the contact force is calculated according to the equality conditions.

The displacement condition requires that the particle is pushed out of the contact area at the next time step, namely

$$(\mathbf{x}^{p,k+1} - \mathbf{x}^{c,k+1}) \cdot \mathbf{n}^c = \frac{d}{2} + r \quad (54)$$

\mathbf{x}^p is updated by

$$\mathbf{x}^{p,k+1} = \mathbf{x}^{p,k} + \Delta t^{k+1/2} \sum_{l=1}^{n_e} \mathbf{v}_l^{k+1/2} N_{lp} \quad (55)$$

and the velocity of node l is updated by

$$\mathbf{v}_l^{k+1/2} = \mathbf{v}_l^{k-1/2} + \Delta t^k \frac{\tilde{\mathbf{f}}_l + N_{lp} F^c \mathbf{n}^c}{m_l} \quad (56)$$

$\tilde{\mathbf{x}}$ and $\tilde{\mathbf{v}}$ are the predicted position and velocity respectively which ignore the influence of contact forces. They are obtained by

$$\tilde{\mathbf{x}}^{p,k+1} = \mathbf{x}^{p,k} + \Delta t^{k+1/2} \sum_{l=1}^{n_e} \tilde{\mathbf{v}}_l^{k+1/2} N_{lp} \quad (57)$$

$$\tilde{\mathbf{v}}_l^{k+1/2} = \mathbf{v}_l^{k-1/2} + \Delta t^k \frac{\tilde{\mathbf{f}}_l}{m_l} \quad (58)$$

Substituting Eqs. (56)–(58) into Eq. (55) gives

$$\begin{aligned} \mathbf{x}^{p,k+1} &= \tilde{\mathbf{x}}^{p,k+1} + \Delta t^k \Delta t^{k+1/2} F^c \mathbf{n}^c \sum_{l=1}^8 \frac{N_{lp}^2}{m_l} \\ \tilde{\mathbf{x}}^{p,k+1} &= \mathbf{x}^{p,k} + \Delta t^{k+1/2} \tilde{\mathbf{v}}^{p,k+1/2} \end{aligned} \quad (59)$$

where

$$\tilde{\mathbf{v}}^{p,k+1/2} = \sum_1^8 N_{lp} \tilde{\mathbf{v}}_l^{k+1/2} \quad (60)$$

is the predicted velocity of the particle. Similarly,

$$\begin{aligned} \mathbf{x}^{c,k+1} &= \tilde{\mathbf{x}}^{c,k+1} - \Delta t^k \Delta t^{k+1/2} F^c \mathbf{n}^c \sum_{j=1}^4 \frac{N_j^2}{m_j} \\ \tilde{\mathbf{x}}^{c,k+1} &= \mathbf{x}^{c,k} + \Delta t^{k+1/2} \tilde{\mathbf{v}}^{c,k+1/2} \end{aligned} \quad (61)$$

Substituting Eqs. (59) and (61) into Eq. (54) gives

$$\begin{aligned} F^c &= \frac{\tilde{m}_p \tilde{m}_c (\tilde{\mathbf{v}}^{c,k+1/2} - \tilde{\mathbf{v}}^{p,k+1/2}) \cdot \mathbf{n}^c}{\Delta t^k (\tilde{m}_p + \tilde{m}_c)} \\ &+ \frac{\tilde{m}_p \tilde{m}_c}{\Delta t^k \Delta t^{k+1/2} (\tilde{m}_p + \tilde{m}_c)} \left(\frac{d}{2} + r - g^c \right) \end{aligned} \quad (62)$$

Similarly, the velocity condition requires

$$(\mathbf{v}^{p,k+1} - \mathbf{v}^{c,k+1}) \cdot \mathbf{n}^c = 0 \quad (63)$$

which leads to

$$F^c = \frac{\tilde{m}_p \tilde{m}_c (\tilde{\mathbf{v}}^{c,k+1/2} - \tilde{\mathbf{v}}^{p,k+1/2}) \cdot \mathbf{n}^c}{\Delta t^k (\tilde{m}_p + \tilde{m}_c)} \quad (64)$$

Compared with Eq. (64), Eq. (62) has an additional term associated with the penetration depth. Because the contact are detected only when Eq. (20) is satisfied, the second term in Eq. (62) is positive. As a result, the resultant contact force based on the displacement condition must be larger than that based on the velocity condition. So the equality in Eqs. (52) and (53) can hardly be reached simultaneously which is because the time discretization makes the displacement in the next step is determined by the velocity. For a single contact pair, the contact force based on the displacement condition makes $(\mathbf{v}^{p,k+1} - \mathbf{v}^{c,k+1}) \cdot \mathbf{n}^c > 0$ which may cause contact force oscillation. On the other hand, the contact force based on the velocity displacement condition cannot push the contact pair away enough so that Eq. (52) is satisfied. A general expression for the resultant contact force can be given by

$$\begin{aligned} F^c &= \frac{\tilde{m}_p \tilde{m}_c (\tilde{\mathbf{v}}^{c,k+1/2} - \tilde{\mathbf{v}}^{p,k+1/2}) \cdot \mathbf{n}^c}{\Delta t^k (\tilde{m}_p + \tilde{m}_c)} \\ &+ \alpha \frac{\tilde{m}_p \tilde{m}_c}{\Delta t^k \Delta t^{k+1/2} (\tilde{m}_p + \tilde{m}_c)} \left(\frac{d}{2} + r - g^c \right) \end{aligned} \quad (65)$$

which is the linear combination of the resultant contact force based on the velocity condition and the displacement condition with a user-defined parameter $0 \leq \alpha \leq 1$.

The value of parameter α is determined empirically. When $\alpha \approx 1$, the displacement condition is satisfied but the normal velocity of the particle and contact surface is discontinuous which leads to severe contact force oscillations. On the other hand, when $\alpha \approx 0$, the contact force oscillations decrease but the contact penetration may appear especially when the contact pair has a large relative velocity. In practice, it is suggested to set a bigger α in

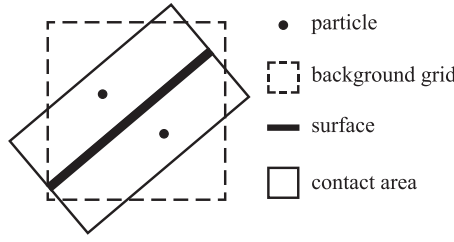


Fig. 9. Two particles contact to a single surface.

the problem with large relative velocity such as the armor piercing simulation and a small α in quasi-static problems. In this paper, α is set to 0.3.

4.2. Contact force iteration

The interaction among contact pairs must be taken into consideration when imposing contact forces. Let m denote the total number of detected contact pairs. Because two contact pairs may share a common particle or finite element, or merely their particles share common background grid nodes, or their elements share common nodes, the contact conditions at these contact pairs

$$(\mathbf{x}_i^{p,k+1} - \mathbf{x}_i^{c,k+1}) \cdot \mathbf{n}_i^c \geq \frac{d_l}{2} + r_l, l = 1, 2 \dots m \quad (66)$$

cannot be satisfied simultaneously by simply imposing the force like Eq. (65) on each contact pair. For example, two particles move into both sides of the contact area of an element face as shown in Fig. 9. Because the two particles locate in the same cell, their contact forces are added onto same nodes. The contact forces imposed on the second particle would pull the first particle back into the contact area so that the contact condition Eq. (66) is not satisfied.

To overcome the difficulties caused by the interaction among the contact pairs to make the contact conditions satisfied for all contact pairs simultaneously, the contact forces must be imposed repeatedly. So an iteration process of imposing contact forces is introduced. In each iterative step, the predicted displacement and velocity are updated which is used to calculate a new contact force for each contact pair by Eq. (65). Only positive contact forces are added to nodal forces because the contact forces should not be negative. The nodal forces, which include the internal forces and contact forces in previous iterative steps, are employed to calculate the predicted displacement and velocity in the next iterative step. The iteration converges when all contact pairs satisfy contact conditions. Fig. 10 gives the flow chart of the iterative process. In most circumstances where the contact situation is rather simple, the convergence can be reached very soon.

5. Numerical results

Several numerical examples are presented in this section to test the performance of the proposed algorithm. Section 5.1 illustrates the elimination of the contact crack and measures the efficiency of the improved local search method. Section 5.2 verifies that the contact penetration is successfully eliminated by the new contact algorithm. Section 5.3 is an application of the non-penetration contact method into 3D airbag simulation. And Section 5.4 presents a wedge falling into water simulation as an example of the FSI problem.

5.1. Validation of the improved local search method

In order to illustrate the contact area and the contact crack of the surfaces, a local search test is given here.

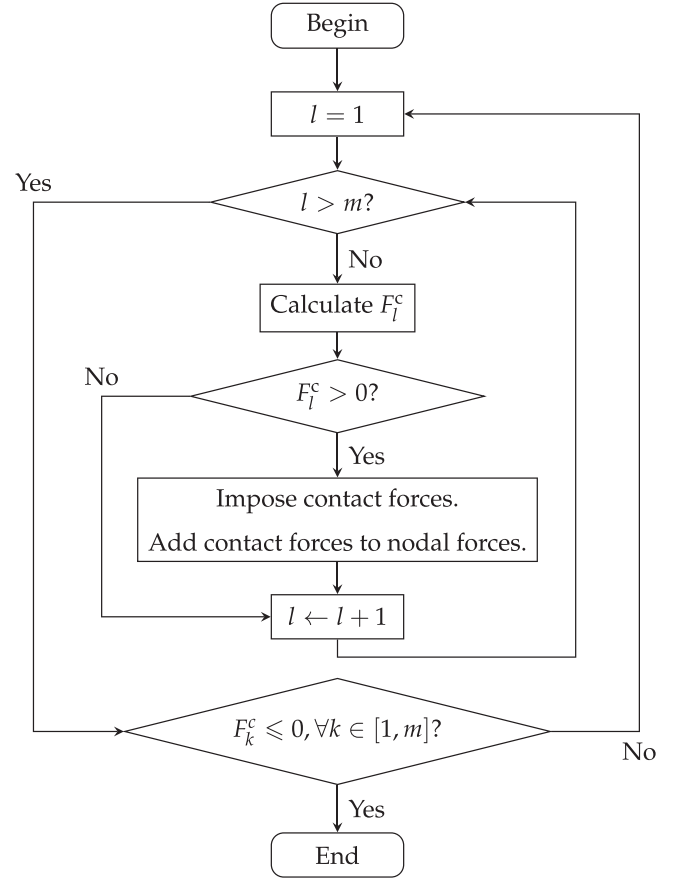


Fig. 10. Iteration process on imposing contact forces.

First of all, we test the contact status of a large number of particles to a given surface. The particles are randomly generated in a cubic $[-1, 1] \times [-1, 1] \times [-1, 1]$. To prevent the surface from being too distorted, the four nodes of the surface are restricted into four quadrants of the cubic respectively. The thickness of the surface is set as 0.24 and 200,000 particles with radius $r = 0.2$ are generated. Fig. 11 shows the contact status of these particles with the surface. In order to highlight the contact area of the surface, the particles which are not detected to contact the surface are not displayed. The particles that contact at the internal position and on the surface edges are represented by solid balls and hollow balls, respectively. Comparing the result of the original local search method (Fig. 11a) with the improved method (Fig. 11b), we can find both methods have similar performance on the internal contact particles, but the particles contacting on the surface edges can only be detected by the improved method.

The local search methods are also tested on two connected surfaces. The particles are also generated in the same cubic as before and two connected surfaces are generated randomly in the middle of the cubic. The test results are shown in Fig. 12. In addition to the contact area extension around the surface edges, the particles in the contact crack around the joint line are also detected to contact to the surfaces by the improved method.

In order to compare the efficiency between the improved local search method and the original method, the CPU time consumed by 1000 tests are compared. In each test, 200,000 random potential contact pairs are examined through a local search method. The CPU time consumed by each test ranges widely because the contact pair is generated randomly. To illustrate the efficiency of the original and the improved local search method, a histogram of the frequency of the CPU time is given in Fig. 13. In the his-

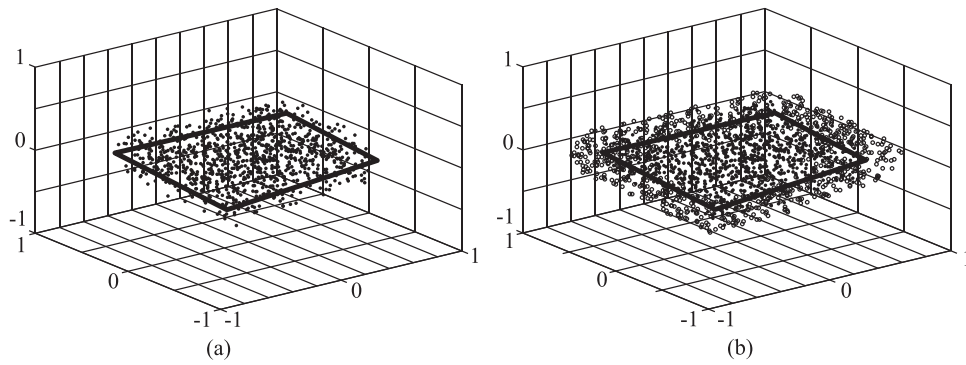


Fig. 11. Contact status of particles with one surface obtained by (a) the original local search method, and (b) the improved local search method.

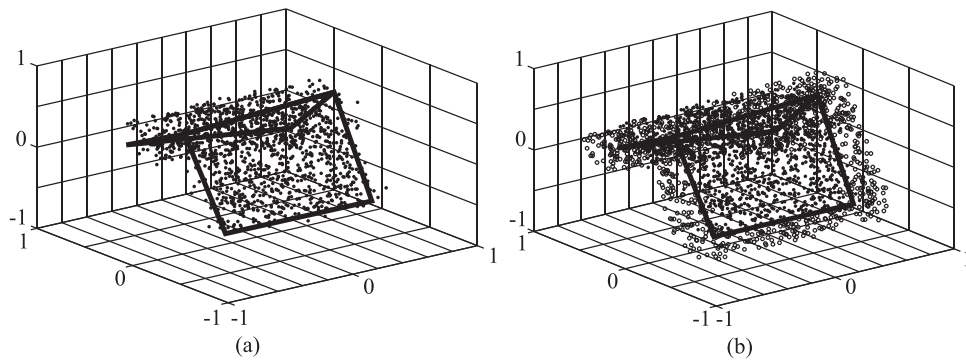


Fig. 12. Contact status of particles with two connected surfaces obtained by (a) the original local search method, and (b) the improved local search method.

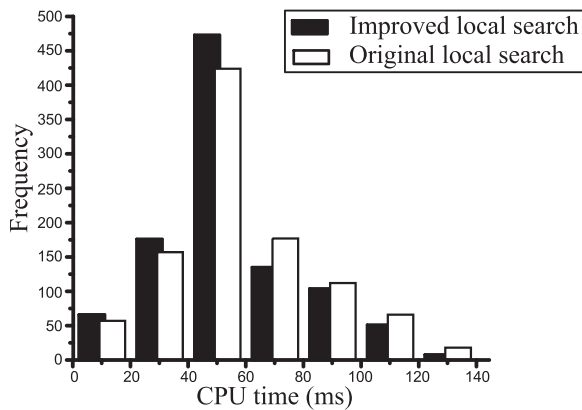


Fig. 13. The CPU time histogram.

togram, solid blocks and hollow blocks represents the number of tests which consume the CPU time within the corresponding range through the improved and original local search method, respectively. For example, there are 474 tests whose CPU time locates in the range $40\text{ms} < t \leq 60\text{ms}$ through the improved local search method. Considering the number of tests whose CPU time is less than 60ms, the number of tests employing the improved method is more than the original method, and vice versa. It indicates that the original method tends to cost more time than the improved method. The main reason is that the improved local search method reaches to convergence earlier because of the criterion (51). As is shown in Fig. 14, because the coordinates of the aim point is limited on the boundary line by the improved method, it reaches to convergence sooner than the original method.

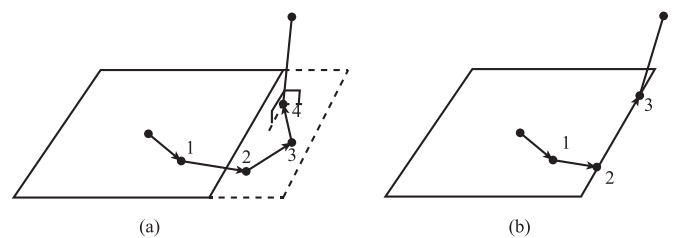


Fig. 14. The iterative process of the original and improved local search method. (a) The original method. (b) the improved method.

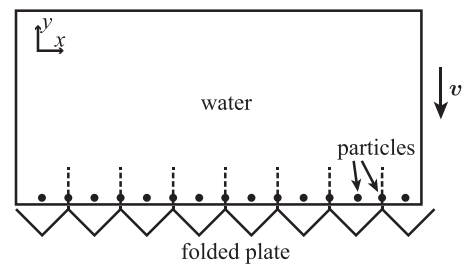


Fig. 15. Water fall onto a folded plate.

5.2. Water falling onto a folded plate

In this section, a quasi-2D FSI example are given to show that he contact penetration phenomenon can be eliminated through the improved local search method.

As is shown in Fig. 15, the water in a block region is discretized with particles and the folded plate is discretized with thin shell elements. In order to test the influence caused by the contact crack,

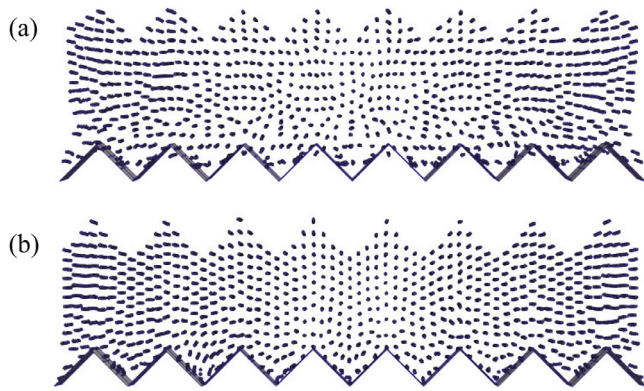


Fig. 16. Particle distribution of the original and improved contact algorithm at the same time. (a) Contact penetration occurs with the original local search method. (b) Contact penetration is eliminated through the improved local search method.

particles are deliberately arranged so that some particles locate exactly above the vertices of the folded plate. The weakly compressible EOS

$$p = (\rho - \rho_0)c_0^2 \tag{67}$$

is employed to model water where p and ρ are the pressure and density of water, $\rho_0 = 1000\text{kg/m}^3$ is the reference density and $c_0 = 50\text{m/s}$ is the artificial sound speed. The folded plate is a rigid body which is fixed at the initial position. When the water impact on the folded plate, its surface would present a zig-zag shape similar as the folded plate.

Fig. 16 shows the particle distribution obtained by both the original and improved contact algorithm at the same time. In the particle distribution of the original contact algorithm, particles above the vertices move through the plate, giving rise to severe contact penetration, as shown in Fig. 16(a). The contact penetration is effectively eliminated through the improved local search method employed as shown in Fig. 16(b).

5.3. Airbag simulation

Contact penetration phenomenon is also observed in 3D simulation. For example, the airbag is widely used in engineering so the airbag simulation is highly demanded in engineering field. Fig. 17 illustrates a typical spherical airbag structure composed of rubber films and bounded with reinforced tapes along longitude and latitude. The reinforced tapes with higher strength and stiffness are sewn onto the airbag in order to eliminate the relative slip.

The rubber films and reinforced tapes are discretized by thin shell elements and cable elements respectively. They are modeled as linear elastic material. For the rubber films $E = 2000\text{MPa}$, $\mu =$

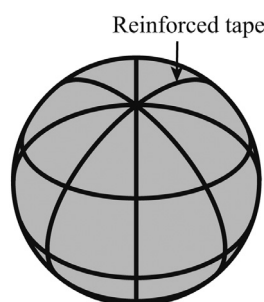


Fig. 17. A typical airbag structure.

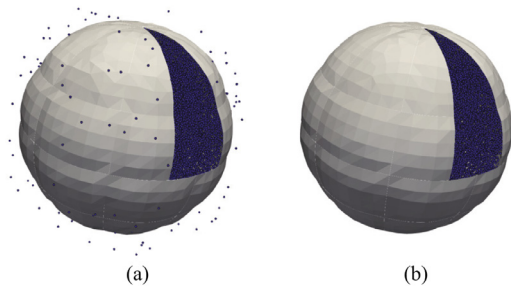


Fig. 18. Airbag simulation results. (a) Severe contact penetration is observed in the original method result. (b) The improved method eliminates the contact penetration.

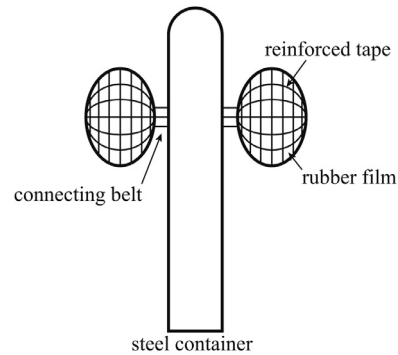


Fig. 19. Steel container with two airbags.

0.3 , $\rho = 1400\text{kg/m}^3$ and for the reinforce tapes $E = 6000\text{MPa}$, $\mu = 0.2$, $\rho = 1400\text{kg/m}^3$. The cable elements connect to the shell elements simply by sharing the same nodes. Air, which is regarded as the ideal gas, is discretized with particles. The atmospheric pressure is imposed on the shell elements as a uniform loading. The reinforced tapes restrict the airbag inflation and as a consequence, the airbag deforms as a watermelon shape. Fig. 18 shows the particle distribution at the same time of the original and improved method. To clarify the simulation model, a part of the rubber films is concealed to expose the air particles. The surface becomes uneven because of the contact force oscillation. The uneven surface give rise to a large amount of contact crack and as a result, severe contact penetration phenomenon is observed in the result of the original contact algorithm as shown in Fig. 18(a). On the contrary, the improved contact algorithm thoroughly eliminates the contact penetration, as shown in Fig. 18(b).

The non-penetration algorithm method has been successfully applied in complex engineering problems. Fig. 19 shows a steel container connected with two airbags which falls into water. The steel container and the airbag films are modeled as thin shell elements. The reinforce tapes and connecting belts are discretized by cable elements. The compressed air in the airbag is modeled as the ideal gas. The weakly compressible EOS is employed to model the water. The steel container, airbag films, reinforced tapes and connecting belt are model as elastic materials. Their material parameters are shown in Table 1.

The airbags are filled with compressed air at the beginning of simulation. In order to impose the initial stress and strain on the airbag film, a relaxation process is conducted. After the relaxation process, the water region and the gravity are activated and the initial velocity is imposed to the falling body. Fig. 20 shows the internal pressure of airbags in the relaxation process. Because of the damping employed in the FEM body, the pressure oscillation decays soon. The deformation is little in the relaxation process. Fig. 21 shows the simulation process with different initial attitudes

Table 1
Material parameters of the falling body.

	Young's modulus (MPa)	Poisson's ratio	Density (kg/m ³)
Steel container	206,000	0.3	7850
Airbag film	2000	0.3	1400
Reinforce tape	6000	0.2	1400
Connecting belt	6000	0.2	1400

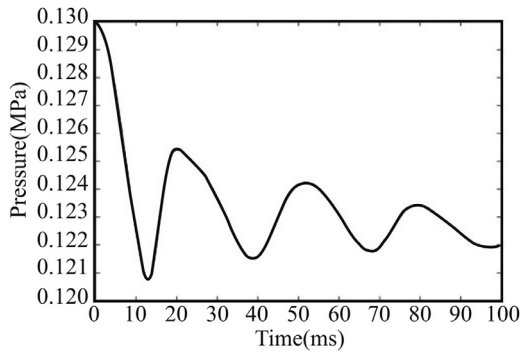


Fig. 20. Internal pressure in relaxation process.

where the color of water particles represents the velocity magnitude. The contact penetration phenomenon have been thoroughly eliminated even in the complex solid-liquid-gas three-phase contact process.

5.4. Wedge falling into water

The wedge falling problem has been widely studied by many researchers. The theoretical solutions in various conditions have been given based on the fully nonlinear velocity potential theory [46]. Zhao et al. [47] also conducted an experiment which serves as a benchmark for numerical simulations. Many computational methods were employed to simulate this problem such as the level set immersed boundary model [48] and the SPH method [49]. Chen [39] has given the velocity curve of the ICFEMP. In this section, the non-penetration contact algorithm are used in the simulation of wedge falling problem to show its accuracy in the FSI problem.

The simulation model is illustrated in Fig. 22. The wedge and water is simulated with finite elements and particles respectively. The rigid wedge is 500 mm in width and 1000 mm in length.

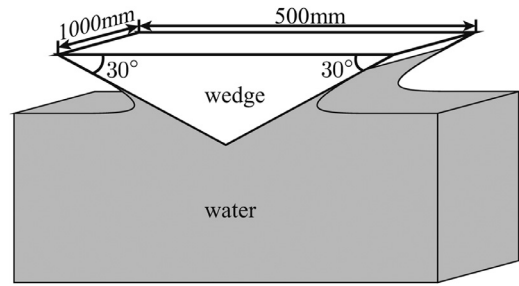


Fig. 22. Free falling of a wedge into water.

The mass of the wedge is 241 kg. The V-shaped section has two 30° dead-rise angles. Water are stored in a tank with a width of 2000 mm and depth of 1000 mm. In the simulation, a plane strain model is employed while the water is modeled by the weakly compressible EOS (67) where p and ρ are the pressure and density of water, $\rho_0 = 1000 \text{ kg/m}^3$ is the reference density and c_0 is the artificial sound speed which is often chosen as 50 m/s to avoid pressure oscillation [50]. The wedge has an initial velocity of -6.51 m/s . The particle spacing and cell size are set as 5 mm and 20 mm respectively, while the average element size is 28 mm. There are 80,000 particles and 171 elements in total for the simulation.

The velocity history of the centroid of the wedge is plotted in Fig. 23. The velocity curve of the ICFEMP with the non-penetration contact algorithm is similar with that of Chen's work [39], which is because the original contact algorithm and the non-penetration contact algorithm use the similar contact forces like Eq. (65). The curve agrees well with the experiment until $t = 0.017 \text{ s}$. At the beginning when the wedge contacts the water, the velocity decreases slower than the experiment result because the contact algorithm is imprecise when the contact region is small. After $t = 0.017 \text{ s}$,

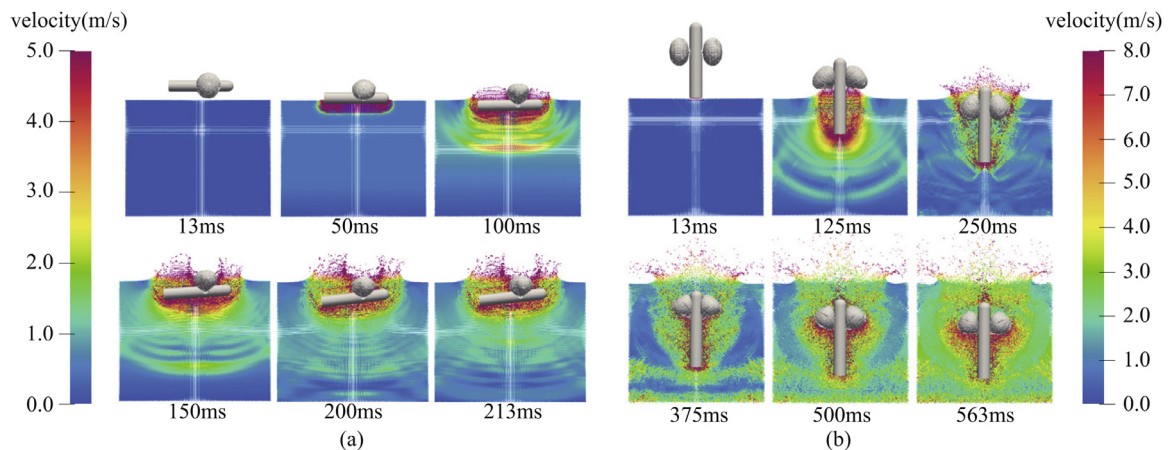


Fig. 21. Simulation process with different initial orientation.

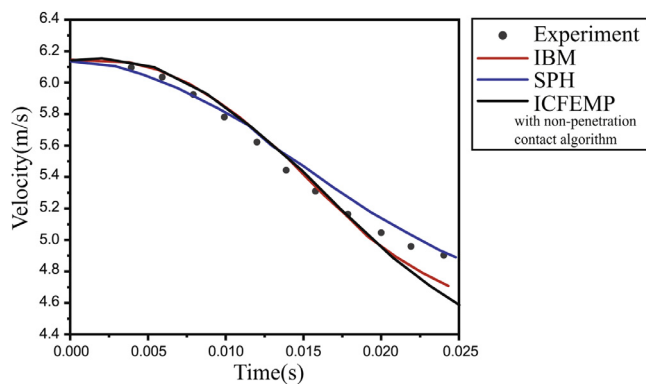


Fig. 23. Velocity history of the falling wedge.

the error increases rapidly because of the weakly compressible EOS and the three-dimensional effects as mentioned by Zhao et al. [47].

6. Conclusion

The particle-to-element contact algorithm employed in ICFEMP method is divided into three steps: global search, local search and imposing contact forces. This paper focuses on the local search step and the way to impose contact forces.

Based on the geometric property of the local search method, it is illustrated that the contact area of two connected elements would not close up in some circumstances which gives rise to the contact crack. The particles in contact crack cannot be detected to contact with the elements. As a result, the contact penetration phenomenon occurs sometimes. An improved local search contact method is proposed in this paper. The contact position is re-defined as the nearest point in the surface to the particle, which turns the local search method into an optimization process. As a consequence, the contact area is extended around the joint line so that the contact crack disappears. Examples are given to show that the improved local search method eliminates the contact penetration thoroughly.

The contact condition is analyzed as well. The velocity condition and the displacement condition leads to different contact forces. The contact force based on the displacement makes the velocity condition satisfied but may increase contact force oscillation. So a general contact force is proposed which is the linear combination of the contact force based on the displacement and velocity condition. However, the contact condition cannot be satisfied simultaneously for all contact pairs by simply imposing forces for each contact pair. In order to overcome the difficulty caused by the interaction among contact pairs, an iterative process of imposing contact forces is proposed. The improved contact algorithm has been successfully applied in the airbag simulation.

Declaration of Competing Interest

The authors declare that they have no known competing financial interests or personal relationships that could have appeared to influence the work reported in this paper.

CRediT authorship contribution statement

Yan Song: Conceptualization, Methodology, Software, Writing - original draft, Writing - review & editing, Validation. **Yan Liu:** Conceptualization, Methodology, Writing - review & editing. **Xiong Zhang:** Conceptualization, Methodology, Writing - original draft, Writing - review & editing, Validation.

References

- [1] Sulsky D, Chen Z, Schreyer H. A particle method for history-dependent materials. *Comput Methods Appl Mech Eng* 1994;118(1):179–96.
- [2] Zhang X, Chen Z, Liu Y. The material point method: a continuum-based particle method for extreme loading cases. Academic Press; 2016.
- [3] Bardenhagen SG, Kober EM. The generalized interpolation material point method. *CMES* 2004;5(6):477–96.
- [4] Sadeghirad A, Brannon RM, Burghardt J. A convected particle domain interpolation technique to extend applicability of the material point method for problems involving massive deformations. *Int J Numer Methods Eng* 2011;86(12):1435–56.
- [5] Song Y, Liu Y, Zhang X. A transport point method for complex flow problems with free surface. *Comput Particle Mech* 2020;7:377–91.
- [6] Steffen M, Kirby RM, Berzins M. Analysis and reduction of quadrature errors in the material point method (MPM). *Int J Numer Methods Eng* 2008;76(6):922–48.
- [7] Sulsky D, Gong M. Improving the material-point method. In: Weinberg K, Pandolfi A, editors. *Innovative numerical approaches for multi-field and multi-scale problems*. Lecture Notes in Applied and Computational Mechanics, 81. Springer; 2016. p. 217–40.
- [8] Chen Z, Hu W, Shen L, Xin X, Brannon R. An evaluation of the MPM for simulating dynamic failure with damage diffusion. *Eng Fract Mech* 2002;69(17):1873–90.
- [9] Gan Y, Sun Z, Chen Z, Zhang X, Liu Y. Enhancement of the material point method using B-spline basis functions. *Int J Numer Methods Eng* 2018;113(3):411–31.
- [10] Huang P, Zhang X, Ma S, Wang H. Shared memory OpenMP parallelization of explicit MPM and its application to hypervelocity impact. *CMES* 2008;38(2):119–48.
- [11] Zhang DZ, Zou Q, VanderHeyden WB, Ma X. Material point method applied to multiphase flows. *J Comput Phys* 2008;227(6):3159–73.
- [12] Ma Z, Zhang X, Huang P. An object-oriented MPM framework for simulation of large deformation and contact of numerous grains. *CMES* 2010;55(1):61–87.
- [13] Huang P, Zhang X, Ma S, Huang X. Contact algorithms for the material point method in impact and penetration simulation. *Int J Numer Methods Eng* 2011;85(4):498–517.
- [14] Zhang DZ, Ma X, Giguere PT. Material point method enhanced by modified gradient of shape function. *J Comput Phys* 2011;230(16):6379–98.
- [15] Lian YP, Zhang X, Liu Y. Coupling of finite element method with material point method by local multi-mesh contact method. *Comput Methods Appl Mech Eng* 2011;200(47–48):3482–94.
- [16] Bardenhagen SG, Nairn JA, Lu H. Simulation of dynamic fracture with the material point method using a mixed J-integral and cohesive law approach. *Int J Fract* 2011;170(1):49–66.
- [17] Daphalapurkar NP, Lu H, Coker D, Komanduri R. Simulation of dynamic crack growth using the generalized interpolation material point (gimp) method. *Int J Fract* 2007;143(1):79–102.
- [18] Chen Z, Feng R, Xin X, Shen L. A computational model for impact failure with shear-induced dilatancy. *Int J Numer Methods Eng* 2003;56(14):1979–97.
- [19] Liang Y, Benedek T, Zhang X, Liu Y. Material point method with enriched shape function for crack problems. *Comput Methods Appl Mech Eng* 2017;322:541–62.
- [20] Sulsky D, Peterson K. Toward a new elastic-decohesive model of arctic sea ice. *Phys D* 2011;240(20):1674–83.
- [21] Sulsky D, Schreyer L. MPM simulation of dynamic material failure with a cohesion constitutive model. *Eur J Mech-A/Solids* 2004;23(3):423–45.
- [22] Lian YP, Zhang X, Zhou X, Ma Z. A FEMP method and its application in modeling dynamic response of reinforced concrete subjected to impact loading. *Comput Methods Appl Mech Eng* 2011;200(17–20):1659–70.
- [23] Lian YP, Zhang X, Liu Y. An adaptive finite element material point method and its application in extreme deformation problems. *Comput Methods Appl Mech Eng* 2012;241:275–85.
- [24] York AR, Sulsky D, Schreyer HL. Fluid–membrane interaction based on the material point method. *Int J Numer Methods Eng* 2000;48(6):901–24.
- [25] Lian YP, Liu Y, Zhang X. Coupling of membrane element with material point method for fluid membrane interaction problems. *Int J Mech Mater Des* 2014;10(2):199–211.
- [26] Bazilevs Y, Takizawa K. *Advances in computational fluid-structure interaction and flow simulation*. Springer; 2017.
- [27] York AR, Sulsky D, Schreyer HL. The material point method for simulation of thin membranes. *Int J Numer Methods Eng* 1999;44(10):1429–56.
- [28] Bardenhagen S, Brackbill J, Sulsky D. The material-point method for granular materials. *Comput Methods Appl Mech Eng* 2000;187(3–4):529–41.
- [29] Bardenhagen S, Guilkey JE, Roessig K, Brackbill J, Witzel W, Foster J. An improved contact algorithm for the material point method and application to stress propagation in granular material. *CMES* 2001;2(4):509–22.
- [30] Hu W, Chen Z. A multi-mesh MPM for simulating the meshing process of spur gears. *Comput Struct* 2003;81(20):1991–2002.
- [31] Homel MA, Herbold EB. Field-gradient partitioning for fracture and frictional contact in the material point method. *Int J Numer Methods Eng* 2017;109:1013–44.
- [32] Moutsanidi G, Kamensky D, Zhang DZ, Bazilevs Y, Long CC. Modeling strong discontinuities in the material point method using a single velocity field. *Comput Methods Appl Mech Eng* 2019;345:584–601.

- [33] Cui X, Zhang X, Sze K, Zhou X. An alternating finite difference material point method for numerical simulation of high explosive explosion problems. *CMES* 2013;92(5):507–38.
- [34] Guilkey J, Harman T, Banerjee B. An Eulerian–Lagrangian approach for simulating explosions of energetic devices. *Comput Struct* 2007;85(11–14):660–74.
- [35] Cui XX, Zhang X, Zhou X, Liu Y, Zhang F. A coupled finite difference material point method and its application in explosion simulation. *CMES* 2014;98(6):565–99.
- [36] Gilmanov A, Acharya S. A hybrid immersed boundary and material point method for simulating 3D fluid–structure interaction problems. *Int J Numer Methods Fluids* 2008;56(12):2151–77.
- [37] Hamad F, Stolle D, Vermeer P. Modelling of membranes in the material point method with applications. *Int J Numer Anal Methods Geomech* 2015;39(8):833–53.
- [38] Cheon Y-j, Kim HG. An efficient contact algorithm for the interaction of material particles with finite elements. *Comput Methods Appl Mech Eng* 2018;335:631–59.
- [39] Chen ZP, Qiu XM, Zhang X, Lian YP. Improved coupling of finite element method with material point method based on a particle-to-surface contact algorithm. *Comput Methods Appl Mech Eng* 2015;293:1–19.
- [40] Wu B, Chen ZP, Zhang X, Liu Y, Lian YP. Coupled shell-material point method for bird strike simulation. *Acta Mech Solida Sin* 2018;31(1):1–18.
- [41] Benson DJ, Hallquist JO. A single surface contact algorithm for the post-buckling analysis of shell structures. *Comput Methods Appl Mech Eng* 1990;78(2):141–63.
- [42] Oldenburg M, Nilsson L. The position code algorithm for contact searching. *Int J Numer Methods Eng* 1994;37(3):359–86.
- [43] Yang B, Laursen TA. A contact searching algorithm including bounding volume trees applied to finite sliding mortar formulations. *Comput Mech* 2008;41(2):189–205.
- [44] Abbo A, Sloan S. A smooth hyperbolic approximation to the Mohr–Coulomb yield criterion. *Comput Struct* 1995;54(3):427–41.
- [45] Bićanić N, et al. Detection of multiple active yield conditions for Mohr–Coulomb elasto-plasticity. *Comput Struct* 1997;62(1):51–61.
- [46] Wu G-X, Xu G-D, Duan WY. A summary of water entry problem of a wedge based on the fully nonlinear velocity potential theory. *J Hydrodyn Ser B* 2010;22(5):859–64.
- [47] Zhao R, Faltinsen O, Aarsnes J. Water entry of arbitrary two-dimensional sections with and without flow separation. In: *Proceedings of the 21st symposium on naval hydrodynamics*, Trondheim, Norway. Washington, DC, USA: National Academy Press; 1996. p. 408–23.
- [48] Zhang Y, Zou Q, Greaves D, Reeve D, Hunt-Raby A, Graham D, et al. A level set immersed boundary method for water entry and exit. *Commun Comput Phys* 2010;8(2):265–88.
- [49] Shao S. Incompressible SPH simulation of water entry of a free-falling object. *Int J Numer Methods Fluids* 2009;59(1):91–115.
- [50] Morris JP, Fox PJ, Zhu Y. Modeling low Reynolds number incompressible flows using SPH. *Journal of Computational Physics* 1997;136(1):214–26. Single velocity field. *Computer Methods in Applied Mechanics and Engineering* 345 (2019) 584–601